Origins of Minimized Lattice Thermal Conductivity and Enhanced Thermoelectric Performance in WS$_2$/WSe$_2$ Lateral Superlattice

Yonglan Hu,[#] Tie Yang,[#] Dengfeng Li, Guangqian Ding,* Chaochao Dun,* Dandan Wu, and Xiaotian Wang*

ABSTRACT: We report a configuration strategy for improving the thermoelectric (TE) performance of two-dimensional transition metal dichalcogenide WS$_2$ based on the experimentally prepared WS$_2$/WSe$_2$ lateral superlattice (LS) crystal. On the basis of density function theory combined with a Boltzmann transport equation, we show that the TE figure of merit zT of monolayer WS$_2$ is remarkably enhanced when forming into a WS$_2$/WSe$_2$ LS crystal. This is primarily ascribed to the almost halved lattice thermal conductivity due to the enhanced anharmonic processes. Electronic transport properties parallel (xx) and perpendicular (yy) to the superlattice period are highly symmetric for both p- and n-doped LS owing to the nearly isotropic lifetime of charger carriers.

Schematic of the WS$_2$/WSe$_2$ lateral superlattice crystal and the p-type figure of merit zT at 300K.

The spin-orbital effect causes a significant split of conduction band and leads to three-fold degenerate sub-bands and high density of states (DOS), which offers opportunity to obtain a high n-type Seebeck coefficient (S). Interestingly, the separated degenerate sub-bands and upper conduction band in monolayer WS$_2$ form a remarkable stair-like DOS, yielding a higher S. The hole carriers with much higher mobility than electrons reveal the high p-type power factor, and the potential to be good p-type TE materials with optimal zT exceeds 1 at 400 K in WS$_2$/WSe$_2$ LS.
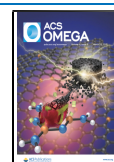
1. INTRODUCTION

Thermoelectric cooling or power generation devices can realize direct conversion between heat and electricity. The efficiency of the thermoelectric (TE) conversion primarily depends on the figure of merit zT of a material, $zT = S^2\sigma T/(\kappa_e + \kappa_l)$, where S, σ, and T are the Seebeck coefficient, electrical conductivity, and absolute temperature, respectively; κ_e and κ_l are the electronic and lattice contribution to thermal conductivity.[1−3] In the past decades, intense effort taken to improve the zT of exiting complex bulk materials seems unsatisfactory since these TE coefficients are strongly coupled, e.g., the S and σ are inversely related, while σ and κ_e are proportionally related.[4−6] Achieving high zT requires high S, high σ, and low thermal conductivity. Thus, new breakthrough in zT lies in how to control these coefficients individually. It has been suggested that low-dimensional DOS could have potential in increasing S without reducing σ; meanwhile, the introduced boundary or interface can scatter phonons and reduce κ_l. These concepts are quite classic and the demonstration was presented in the seminal papers by Hicks and Heremans.[7−9] Nowadays, exploring competitive zT in low-dimensional nanocrystals becomes a promising scenario in a TE community. Potential candidates, such as 2D transition metal dichalcogenides (TMDCs),[10] phosphorene,[11] silicene,[12] bismuth oxyselenide,[13] have been widely investigated.

2D TMDCs draw growing interest in TE due to their superior stability and high carrier mobility. It has been found that the TE performance of 1T-type TMDCs ($MS(Se)_2$, M = Ti, Zr) are much higher than the 2H-type TMDCs ($MS(Se)_2$, M = Mo, W). For example, the optimal zT of monolayer ZrS$_2$ at 300 K is about 1.7,[14] while it is less than 0.1 in monolayer MoS$_2$.[15] Such a great difference in TE performance arises from the distinct phonon transport behaviors, i.e., the κ_l at 300 K for monolayer ZrS$_2$ and MoS$_2$ are 3.29 and 83 W/mK,[14,15] respectively. Based on Gu and Yang,[16] the high κ_l of 2H TMDCs monolayers comes from two crucial factors: (i) The strong bonding stiffness leads to a large span of phonon frequency and therefore the high phonon velocity, and (ii) the large atomic weight difference causes a wide frequency gap, which forbids the anharmonic phonon scattering processes. Similar results were also found in monolayer WSe$_2$ and MoSe$_2$ according to the investigation of Kumar and Schwingenschlögl.[17] As the controlling synthesis of 2H TMDC

monolayers is now a mature technology, improving their TE performance is important for their potential application in TE devices, which in turn lies in how to break their lower limit of κ_l by introducing additional impurities or interfaces.

Interestingly, Duan et al.[18,19] reported the lateral epitaxial growth of 2D heterostructures and superlattices based on 2D TMDCs, and the WS_2/WSe_2 and $MoS_2/MoSe_2$ lateral superlattices (LSs) were well prepared. In addition, a variety of combination of LS, such as MoS_2-WS_2[20] and WSe_2-MoS_2,[21] were also experimentally prepared, and it is possible to turn their morphological or electronic properties. Li et al.[22] even theoretically considered the combination of Janus monolayer with LS crystal (MoSSe and WSSe). On the basis of the theory of low-dimensional TE transport and this experimental realization, it is desirable to improve the TE performance of 2H TMDC monolayers by forming such LS crystal. As demonstrated by Hicks and Dresselhaus,[7] the quantum-well superlattices can alter zT since carriers are confined to move in well, while the interfaces can scatter the phonons. We have shown that the κ_l in $MoS_2/MoSe_2$ LS is greatly minimized due to enhanced phonon scattering rates, as compared to the pristine monolayers.[23] Liu et al.[24] also reported the high TE performance in graphene/boron-nitride LS ascribing to the same mechanism. To date, exploring the TE transport in LS crystals based on existing 2D monolayers is lacking, and mechanisms behind are still not fully understood. Although we have preliminary investigated the phonon transport in $MoS_2/MoSe_2$ LS, the mechanisms of electronic transport and full TE performance of LS are still unclear. Here, we report the TE transport performance of monolayer WS_2 and WS_2/WSe_2 LS. We find that the noticeable inhibited phonon transport and almost remained electronic transport in WS_2/WSe_2 LS with the enhanced zT exceeds 1 at 400 K in p-doped LS.

2. COMPUTATIONAL DETAILS

To obtain the stable structure with fully relaxed lattice parameters and atomic positions, we carry out first-principles calculations within the framework of density functional theory (DFT) using the projector augmented wave (PAW)[25] formalism and the generalized gradient approximation (GGA) Perdew−Burke−Ernzerhof (PBE)[26] exchange-correlation functional, as implemented in VASP.[27] The plane-wave cutoff energy is 400 eV and the Monkhorst-Pack k-points are $9 \times 15 \times 1$ and $7 \times 21 \times 1$ for monolayer WS_2 and WS_2/WSe_2 LS, respectively. The convergence criterion of the self-consistent loop is 10^{-6} eV. The lattices and positions are fully relaxed until the maximum force becomes less than 0.01 eV/Å. We determine that the unit cell parameters $a(b)$ for monolayer WS_2 and WS_2/WSe_2 LS are 5.48(3.16)Å and 11.24(3.25)Å, respectively. When calculating the electronic band structure, the Monkhorst-Pack k-points are increased to $19 \times 31 \times 1$ and $17 \times 57 \times 1$ to guarantee converged TE coefficients. In addition, the spin-orbital coupling (SOC) and modified Becke−Johnson (MBJ) functional are also considered to yield the accurate dispersion and band gap. The MBJ functional shows advantages of time-saving and excellent accuracy on a pair with Heyd−Scuseria−Ernzerhof (HSE) and GW methods, and it is also a suitable approach for predicting full band dispersion when limited experimental data are available, according to Kim et al.[28]

The electronic transport coefficients are calculated using the Boltzmann transport equation (BTE) in a constant relaxation time approximation (CRTA) as implemented in BoltzTraP.[29]

A rigid band approximation[30] is used to treat doping; the Fermi level shifts up for n-type doping, while down for p-type. The S, σ, and κ_e are obtained by solutions of the BTE in terms of the transport distribution function:
$$\sum(\varepsilon) = \sum_{\vec{k}} v_{\vec{k}}^2 \tau_{\vec{k}} \delta(\varepsilon - \varepsilon_{\vec{k}}),[31]$$
where $v_{\vec{k}}$ is the group velocity of carriers with wave vector $\vec{k}$, $\tau_{\vec{k}}$ is the carrier's lifetime, and $\varepsilon_{\vec{k}}$ is the dispersion relation for the carriers.

The κ_l is calculated by solving the phonon BTE as implemented in ShengBTE.[32−34] A linearized pBTE can be defined when considering two- and three-phonon processes as the scattering sources, and the scattering from isotopic disorder is also included in this method. Harmonic and anharmonic interatomic force constants (IFCs) are quite necessary inputs for pBTE, which are obtained from DFT calculations using converged $3 \times 3 \times 1$ and $2 \times 5 \times 1$ supercells for monolayer WS_2 and WS_2/WSe_2 LS, respectively. A converged cutoff distance of 0.6 nm for interactive distance is used in calculating anharmonic IFCs. The harmonic IFCs are obtained by using the Phonopy code.[35] For obtaining anharmonic IFCs and for solving pBTE, we employ the ShengBTE code,[32] based on an adaptive smearing approach to the conservation of energy and on an iterative solution method. It is worthwhile to note that the four-phonon scattering is not considered in present calculations since it usually plays a significant role at a high temperature and for ultrahigh-thermal conductivity materials, according to Feng et al.[36] In addition, since the volume is not a well-defined quantity in 2D crystal, a thickness of $h = 6.2155$ Å is applied, which is equal to the layer separation of bulk WS_2.[6]

3. RESULTS AND DISCUSSION

Monolayer WS_2 and WSe_2 belong to the 2D hexagonal 2H-MoS_2-type TMDCs, as shown in Figure 1a; the unit cell
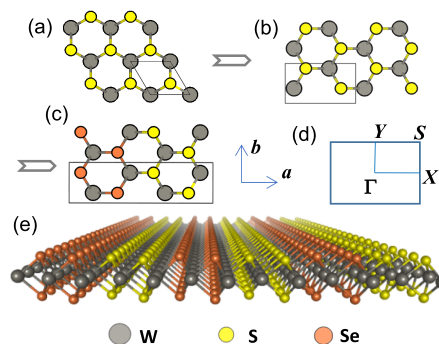

Figure 1. Schematic of the monolayer WS_2 and WS_2/WSe_2 LS. Panels (a) and (b) show the schematic diagram of monolayer WS_2 with hexagonal crystal and rebuild orthorhombic crystal, respectively. Panel (c) is the constructed WS_2/WSe_2 LS structure, which can be obtained by replacing two S atoms with Se in a 2×1 supercell of monolayer WS_2. Noting that the a axis (xx) and b axis (yy) are parallel (armchair) and perpendicular (zigzag) to the superlattice period, respectively. Panel (d) shows the Brillouin zone high-symmetry points, and (e) is the extended view of WS_2/WSe_2 LS.

comprises a S(Se)−W−S(Se) sandwich atomic sequence, and the two S(Se) atoms are symmetrical to the hexagonal W−W plane, which were experimentally prepared by Lan and Huang,[37,38] respectively. Different from graphene, both WS_2 or WSe_2 monolayers are semiconductors with a direct band gap of about 1.55[39] and 1.56 eV,[17] respectively; hence, they draw growing interest in electronic and optical devices. They

are also highlighted as potential TE materials due to their superior stability and high carrier mobility, unfortunately, the high κ_l in the crystals overshadows these advantages with the optimal zT less than 0.1 at room temperature.[17,39] We set out to turn the TE transport properties by using a model of the LS structure. In order to construct a WS_2/WSe_2 LS, we first rebuilt the hexagonal crystal of monolayer WS_2 in an orthorhombic crystal, as shown in Figure 1b, which allows us to explore the TE transport along the armchair (xx) and zigzag (yy) directions. Then, the LS is formed by replacing two S atoms with Se in a 2×1 supercell of the orthorhombic crystal, forming a superlattice period along xx, as shown in Figure 1c. Based on our previous study,[23] the κ_l in $MoS_2/MoSe_2$ LS is greatly minimized as compared to the pristine monolayers. Thus, we expect to alter the TE performance of WS_2 or WSe_2 monolayers through the similar mechanism.

The calculated SOC-MBJ band structure and DOS of monolayer WS_2 and WS_2/WSe_2 LS are shown in Figures 2a,b,
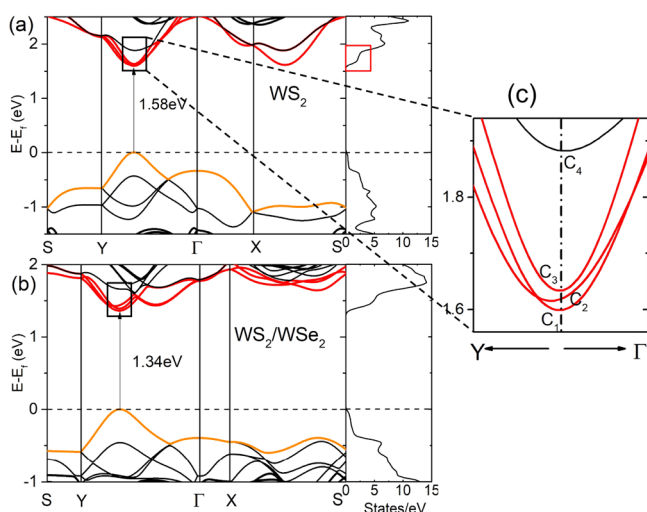
Figure 2. Calculated electronic band structure and density of states (DOS) of (a) monolayer WS_2 and (b) WS_2/WSe_2 LS along the symmetry directions of the Brillouin zone with SOC effect and MBJ functional included. (c) Conduction bands near the Fermi energy. The red box labeled in (a) shows the remarkable stair-like DOS at the conduction band minimum of monolayer WS_2.

respectively. The calculated band gap of 1.58 eV for monolayer WS_2 is in agreement with a reported value of 1.55eV,[39] and it is smaller (1.34 eV) for WS_2/WSe_2 LS. The uppermost valence band and the low-lying conduction bands relative to the Fermi level, which individually determines the hole and electron transport properties, both primarily arise from the W|d > and S|p > states for monolayer WS_2, while for WS_2/WSe_2 LS, they in addition come from Se|p > states, as the projected DOS is shown in Figure S1. A closer look over the band structure reveals that the SOC effect leads to a markedly split of the conduction band, while the valence band seems unaffected; this SOC-induced band splitting primarily arises from the d orbital splitting of transition metal W when it bonded to ligands S or Se, according to Li et al.[40] Importantly, the split leads to a three-fold degenerate lowest-energy C_1, C_2, and C_3 sub-bands in both monolayer WS_2 and WS_2/WSe_2 LS, as shown in Figure 2c, which leads to the high conduction DOS. According to Pei et al.,[41] a highly degenerate level of the electronic band will optimize the electronic performance

through the increased factor N_v, which in turn increases the DOS effective mass ($m^* = N_v^{2/3}m_b^*$) without explicity reducing carrier mobility μ, as the μ is low for heavy band mass. In particular, the degenerate three sub-bands separate in energy to the upper C_4 conduction band, giving rise to a remarkable stair-like DOS and playing an important role in electronic transport.

The electronic transport coefficients are calculated by the BTE within a CRTA. Within the CRTA, the σ and κ_e can only be calculated with a constant relaxation time (τ) included, while τ is canceled in eq 2 of S. Thus, S can be directly calculated from the DFT band structure, but the evaluation of σ and κ_e still requires the knowledge of τ.[42] Here, we employ the deformation potential (DP) theory[43] of Bardeen and Shockley to calculate τ, which is generalized to include the scattering of carriers by acoustic modes and allows to evaluate τ in terms of the DP constant (E_l), elastic constant (C_{2D}), and effective mass (m^*). Based on these parameters, the carrier mobility can be obtained according to the following formula:

$$\mu = \frac{e\hbar^3 C_{2D}}{k_B T m^* m_d^* E_l^2} \tag{1}$$

The relaxation time τ is given by,

$$\tau = \frac{\mu m^*}{e} \tag{2}$$

Where $C_{2D} = \frac{1}{S_0}\frac{\partial^2 E}{\partial(\Delta l/l_0)^2}$, a second order of the total energy with respect to deformation, $\Delta l/l_0$, and $E_l = \frac{\partial E_{edge}}{\partial(\Delta l/l_0)}$, the slope of the band-edge energies with respect to $\Delta l/l_0$, and $m_d^* = \sqrt{m_{\Gamma-X}^* m_{\Gamma-Y}^*}$. Calculated results are shown in Figure S2 and Table 1.

Table 1. DP Constant, Elastic Modulus, Carrier Effective Mass, Carrier Mobility, and Carrier Relaxation Time at 300 K[a]

LS[a]			E_l (eV)	C_{2D} (eVÅ^{-2})	m^* (m_e)	μ (cm^2 V^{-1} s^{-1})	τ (10^{-14} s)
WS_2	n	xx	−9.25	9.15	0.27	229.37	3.51
		yy	−9.23	9.16	1.27	49.03	3.53
	p	xx	−2.44	9.15	1.01	799.87	45.78
		yy	−2.45	9.16	0.42	1909.91	45.46
WS_2/WSe_2	n	xx	−9.08	8.18	0.4	119.36	2.71
		yy	8.18	8.31	1.27	40.57	2.92
	p	xx	−2.39	8.18	1.19	604.67	40.77
		yy	2.47	8.31	0.39	1754.88	38.78

[a]Both electrons and holes along different directions are calculated.

Although the DP theory shown reliability for calculation of τ, we still need to discuss the possible challenges of this theory here since it just consider acoustic phonon scattering on carriers, which in some cases will overestimate τ. For WS_2/WSe_2 LS, the increase of atoms in the unit cell leads to a large number optical modes, as shown in Figure 4b, and the acoustic modes are coupled with low-lying optical modes. However, these optical modes are almost linear dispersion except for the ZO, TO, and LO modes, which mean that possible scattering on carriers may arise from these low-frequency optical

phonons. From monolayer WS$_2$ to WS$_2$/WSe$_2$ LS, the polar optical phonon (POP) scattering should be checked as the introduced small dipole. According to Hung *et al.*,[44] the strength of electron−POP coupling mainly arises from the phonons with frequency separation around LO and TO modes, which can be quantified by a ratio of ω_L/ω_T, where ω_L and ω_T are the frequencies of LO and TO modes. A clear view of the LO and TO modes are shown in Figure S3. A significant frequency separation along Γ-X and Γ-Y is found for monolayer WS$_2$, while the separation along X−S−Y is significant for WS$_2$/WSe$_2$ LS. Taking averaged ω_L and ω_T values, we determine the the ratios of ω_L/ω_T for monolayer WS$_2$ and WS$_2$/WSe$_2$ LS are 1.09 and 1.08, respectively, which might explain the unconspicuous POP effect in the LS crystal, as compared to monolayer WS$_2$. In addition, the τ usually decreases with the reduction of dimensionality due to the quantum confinement, in a nonpolar case that could be reflected by the enhanced DOS near the Fermi level. Based on the Fermi golden rule for a nonpolar case, the relation $\tau^{-1} \propto$ DOS can be defined.[45] Therefore, the higher DOS near the Fermi level (see Figure 2b) indicates the enhanced quantum confinement in WS$_2$/WSe$_2$ LS, and hence leads to the decreased τ (see Table 1). In addition, the higher hole τ is in accordance with the lower valence DOS.

The calculated E_l and C_{2D}, as shown in Table 1, are nearly independent of the structural orientation. Thus, the highly asymmetric carrier mobility along xx and yy comes from the anisotropic effective mass. It is regularly found that electrons with higher m^* along yy leads to the lower μ in this direction, while holes instead with lower m^* along yy leads to the higher μ in this direction. Although μ is highly anisotropic, the calculated relaxation time τ is almost isotropous since it only depends on E_l and C_{2D} with m^* excluded according eqs 4 and 5. Based on the Mott relation, σ and S in eqs 1 and 2 can be simplified as follows[8]:

$$\sigma(\varepsilon) = n(\varepsilon)e\mu(\varepsilon) = n(\varepsilon)e^2\frac{\tau(\varepsilon)}{m^*} \tag{3}$$

$$S = \frac{\pi^2}{3}\frac{k_B^2 T}{q}\left(\frac{d[\ln(\sigma(\varepsilon))]}{dE}\right)_{E=E_F}. \tag{4}$$

For similar τ, higher μ (lower m^*) means a longer mean free path, which usually indicates a smaller carrier density $n(\varepsilon)$. Therefore, there could be a vanishing anisotropy in electronic transport. In addition, one can also notice from Table 1 that the DP results for monolayer WS$_2$ and WS$_2$/WSe$_2$ LS are very similar. For parabolic bands, the transport distribution can be defined in a simpler form: $\sum(\varepsilon) = g(\varepsilon)v(\varepsilon)^2\tau(\varepsilon)$,[31] where $g(\varepsilon)$ is the DOS. As a result, the similar DOS, μ, and τ could result in small anisotropic of electronic transport coefficients between monolayer WS$_2$ and WS$_2$/WSe$_2$ LS. Moreover, it is important to emphasize that the much lower p-type E_l, which reflects the minimal sensitivity of the valence band maximum to deformation, leads to the extremely high μ for holes, as compared to electrons. It is expected to obtain a better p-type TE performance from this high hole mobility.

Electronic transport coefficients at 300K along xx and yy as a function of hole and electron density are shown Figure 3. We find here the nearly vanishing anisotropy and the much closer performance between monolayer WS$_2$ and WS$_2$/WSe$_2$ LS. It is important to note that the S shown in Figure 3a,b is quite large at 300 K with a value of 552 μV/K for monolayer WS$_2$ at a
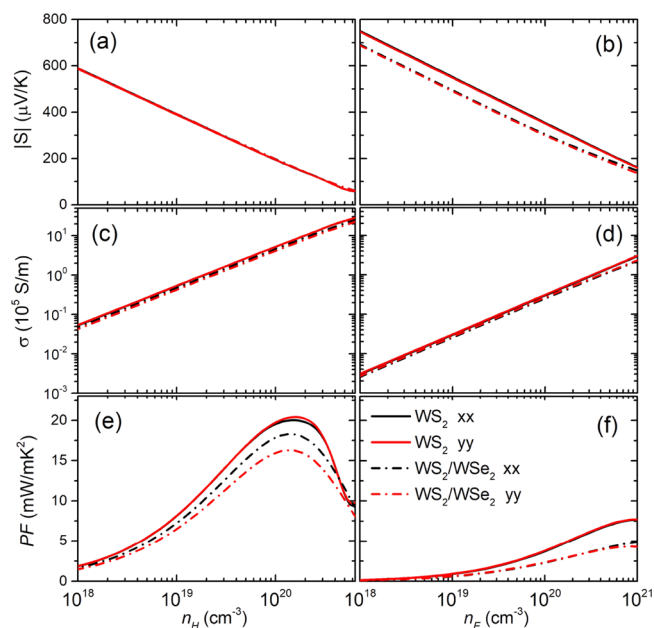
**Figure 3.** Electronic transport coefficients of monolayer WS$_2$ and WS$_2$/WSe$_2$ LS parallel (xx) and perpendicular (yy) to the superlattice period at 300 K. The left and right panels denote the p- and n-doped performance, respectively. (a, b) The Seebeck coefficient (S), (c, d) the electrical conductivity (σ), and (e, f) the power factor (PF = $S^2\sigma$).

typical electron density of 10^{19} cm^{-3}. The n-type S is higher than p-type primarily due to the high conduction DOS arising from the three-fold degenerate sub-bands, according to Pei *et al.*[41] From eqs 6 and 7, the S can be enhanced from an increased energy-dependence of carrier density d$n(\varepsilon)$/dε, which can be achieved by enhancing the dependence of DOS on energy, d$g(\varepsilon)$/dε.

Consequently, the prominent stair-like conduction DOS of monolayer WS$_2$ accounts for its higher n-type S, as shown in Figure 3b. In contrast to S, the p-type σ is much higher than the n-type due to the extremely high μ of holes, see in Figures 3c,d. It is also detectable that the σ of monolayer WS$_2$ is a little higher than WS$_2$/WSe$_2$ LS due to its higher μ. Finally, the power factors (PF = $S^2\sigma$) are given in Figure 3e,f; it is interesting that high n-type S as originated from the three-degenerate sub-bands does not overcome the lower n-type σ and leads to the low n-type PF. Instead, due to the extremely high hole mobility, the high p-type σ accounts for the high p-type PF. The optimal PFs are about 20.5 and 18.4 mW/mK^2 for p-doped monolayer WS$_2$ and WS$_2$/WSe$_2$ LS, respectively, which are higher than monolayer MoS$_2$,[15] WSe$_2$,[17] and even the star bulk material Bi$_2$Te$_3$.[29] The calculated κ_e shown in Figure S4 is less than 0.5 W/mK at a carrier density of 10^{19} cm^{-3}; thus, the thermal conductivity should be dominated by lattice contribution.

Now, we set out to discuss the phonon transport properties in monolayer WS$_2$ and WS$_2$/WSe$_2$ LS. Like other 2H TMDC monolayers, monolayer WS$_2$ and WSe$_2$ possess high κ_l also because of the wide frequency gap and the strong bonding stiffness, which leads to the long relaxation time and high group velocity. The theoretical κ_l of WS$_2$ and WSe$_2$ monolayers at 300 K are higher than 100 and 50 W/mK,[17,39] respectively. It is worthwhile to note that these values are based on the hexagonal crystals (Figure 1a) and a single-mode CRTA of the BTE. The smaller span of phonon frequency, as arising from
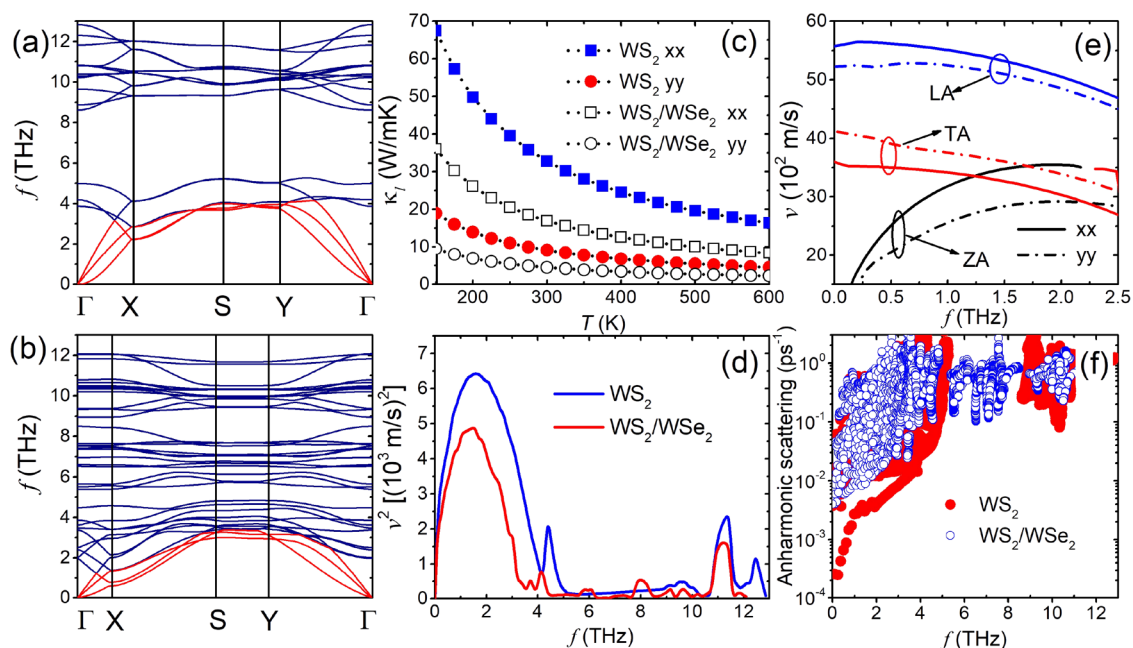
Figure 4. Phonon transport coefficients and performance. Panels (a) and (b) show the calculated phonon dispersion of monolayer WS_2 and WS_2/WSe_2 LS; the two transverse (ZA, TA) and one longitudinal (LA) acoustic branches are highlighted in red. Calculated lattice thermal conductivity with respect to temperature is given in (c), and (d) shows the averaged square of phonon velocity of monolayer WS_2 and WS_2/WSe_2 lateral superlattice. (e) Acoustic phonon velocity (ZA, TA, LA) of monolayer WS_2 along different directions. (f) Comparison of the anharmonic phonon scattering rate at 300 K.

the heavier atomic mass of Se and the smaller elastic constant leads to the lower κ_l of WSe_2 monolayer. In order to minimize κ_l, it is desirable to manipulate the frequency gap by alloying the two pristine monolayers, which could be realized by using the LS structure as a building block.

The calculated phonon spectra with vanishing imaginary frequency for monolayer WS_2 and WS_2/WSe_2 LS are shown in Figure 4a,b, respectively, which also points to the stability of the synthesized monolayer and LS. Due to the formula $(WS_2)_2$ of the rebuild orthorhombic monolayer WS_2, there are three acoustic branches and 15 optical branches, which is a little different from the one based on hexagonal crystal.[39] The lowest ZA acoustic branch corresponds to the out-of-plane displacement, while the higher TA and LA branches correspond to the in-plane transverse and longitudinal displacements. In general, the acoustic branches do most of the contribution to κ_l, while the large number of optical branches instead has little contribution. Based on Ouyang *et al.*,[39] the optical contribution to κ_l in monolayer WS_2 is less than 1%. Due to the large atomic weight difference between W and S, there is a wide frequency gap between acoustic branches and high optical branches, which partly forbids the anharmonic processes. However, for WS_2/WSe_2 LS, one can see that the acoustic branches are coupled with low-lying optical branches.

The κ_l of monolayer WS_2 along armchair (xx) and zigzag (yy) directions are 33.8 and 9.2 W/mK, respectively, as plotted in Figure 4c. The xx and yy directions are both the principle axis of the κ_l tensor because of the orthorhombic symmetry crystal. The κ_l is inversely proportional to the temperature ($\kappa_l \propto 1/T$) since the phonon–phonon interaction is enhanced with the increasing temperature. In contrast to the isotropic κ_l in hexagonal crystal, we obtain here the strong anisotropic κ_l along xx and yy directions, which can be better understood from the anisotropy of group velocity (v). The v values of ZA, TA, and LA acoustic branches are plotted in Figure 4e; it is

clear that the v has a significant difference along xx and yy directions for all three acoustic branches. Both ZA and TA branches exhibit higher v along the xx direction, while the TA branch shows higher v along the yy direction. At a low-frequency limit, the v of the quadratic ZA branch approaches to zero at the Γ point, and the v in xx and yy directions are 36 and 41 ($\times 10^2$ m/s) for the TA branch, and 56 and 52 ($\times 10^2$ m/s) for the LA branch, with an anisotropy of 1.1 and 1.08, respectively. The v of the LA branch is quite higher than ZA and TA branches, which plays dominate contribution to κ_l. Therefore, the anisotropy of κ_l arises from all three acoustic branches, and the higher κ_l in the xx direction is mainly contributed to the ZA and LA branches.

The calculated κ_l values for WS_2/WSe_2 LS at 300 K, as presented in Figure 4c, are 16.9 and 4.5 W/mK along xx and yy directions, respectively. It is important that these values are nearly halved as compared to monolayer WS_2, which can be ascribed to the enhanced anharmonic three-phonon processes coming from the enhanced coupling between acoustic and optical branches. From Figure 4f, one can notice that the scattering probability of acoustic phonons and low-lying optical phonons (below 5 THz) in WS_2/WSe_2 LS is remarkably higher than that in monolayer WS_2. The enhanced anharmonic processes usually include the absorption and emission processes, in which two incident phonons with energy are combined into one phonon, or one incident phonon is split among two phonons. In addition, we calculate the averaged square of v, $v_\omega^{2,\alpha} = \sum_\lambda v_\lambda^{2,\alpha} \delta(\omega - \omega_\lambda)/\sum_\lambda \delta(\omega - \omega_\lambda)$,[46] as plotted in Figure 4d. Obviously, the v_ω^2 of WS_2/WSe_2 LS is quite lower than monolayer WS_2, which can be understood by the weaker bonding stiffness in WS_2/WSe_2 LS as confirmed by its smaller C_{2D} in Table 1. A weaker bonding stiffness causes a smaller span of frequency and leads to the smaller group velocity. It can be also observed from Figure 4d that the low-frequency phonons (below 5 THz) dominate the

contribution to κ_l. As a result, we achieve the minimized κ_l in WS$_2$/WSe$_2$ LS as compared to the pristine monolayers.

In order to discuss the anisotropic κ_l in terms of the chemical bonding strength, we calculate the longitude IFCs of corresponding bonds in the unit cell, as labeled in Figure S5. In the finite displacement method, potential energy is represented as a function of atomic position, $V[r(j_1),..., r(j_n)]$, based on which the IFCs is given by

$$\Phi_{\alpha\beta}(j, j') = \frac{\partial^2 V}{\partial r_\alpha(j)\partial r_\beta(j')} \tag{5}$$

where α and β are the Cartesian indices, j and j' are the indices of atoms, and $\partial r_\alpha(j)$ is the finite displacement of the j-th atom along the α direction. Calculated IFCs for both monolayer WS$_2$ and WS$_2$/WSe$_2$ LS are shown in Table 2. Φ_1 corresponds

Table 2. Interatomic Force Constants (IFCs) for Monolayer WS$_2$ and WS$_2$/WSe$_2$ LS[a]

LS	Φ_1 (Ry/bohr^2)[a]	Φ_2 (Ry/bohr^2)	Φ_3 (Ry/bohr^2)
WS$_2$	5.461	4.685	4.685
WS$_2$/WSe$_2$	4.812	4.038	4.408

[a]Φ_1, Φ_2, and Φ_3 are the IFCs for bond 1 along xx, bond 2 and bond 3 along yy, respectively.

to IFC of bond 1 along the xx (armchair) direction, while Φ_2 and Φ_3 correspond to IFCs of bond 2 and 3 along the yy (zigzag) direction. A large IFC means a strong chemical bonding stiffness, which leads to the severe atomic vibration and high κ_l. As shown in Table 2, in comparison to Φ_2 and Φ_3, the higher Φ_1 is in accordance with the higher κ_l along the xx direction. Meanwhile, these IFCs are weakened when forming the WS$_2$/WSe$_2$ LS, which also points to the enhanced anharmonicity and minimized κ_l in LS crystal.

With all TE coefficients available, we now evaluate the figure of merit zT for both monolayer WS$_2$ and WS$_2$/WSe$_2$ LS. Figure 5 shows the evaluated zT at 300 K as a function of carrier density. It is found that that p-type zT is much higher than the n-type due to the excellent hole transport performance. Importantly, we achieve the enhanced zT in WS$_2$/WSe$_2$ LS as contributed by the minimized κ_l. The lower κ_l in the yy direction leads to the better TE performance. The optimal p-type zT of monolayer WS$_2$, as shown in Figure 5a, are 0.16 and 0.47 along xx and yy, respectively, which are higher than that of monolayer MoS$_2$,[15] MoSe$_2$, and WSe$_2$[17] (less than 0.1). In WS$_2$/WSe$_2$ LS, the optimal p-type zT increases to 0.28 and 0.68 along xx and yy, respectively; this value (0.68) is comparable to the maximum zT ($\sim$0.7) of commercial PbTe,[47] which is also a record value among 2H TMDC monolayers. The inset in Figure 5b shows the optimal p-type zT of WS$_2$/WSe$_2$ LS with respect to temperature. With the increasing temperature, the optimal zT along xx and yy can exceed 1 at a threshold temperature around 550 and 400 K, respectively, indicating the potential as a candidate for p-type TE materials working under a moderate temperature. It is known that the experimental thermal conductivity is usually lower than the theoretical one since the experimental samples inevitably contain defects, distortion, and impurities. Despite the possible overestimation of τ by DP theory, we expect that such promising zT could be realized experimentally.

Before closing, the following three facts should be noted: (i) It is believed that the band degeneracy is an important feature
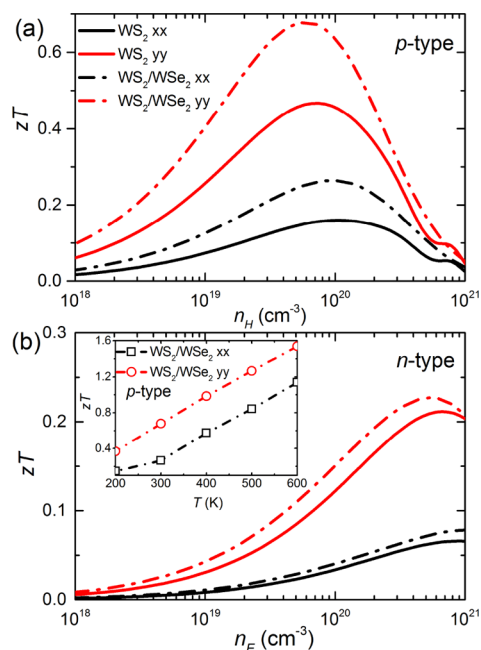
Figure 5. Calculated thermoelectric figure of merit zT at 300 K as a function of (a) hole and (b) electron density. The inset in (b) shows the temperature-dependent optimal p-type zT of WS$_2$/WSe$_2$ LS.

for enhanced PF, as the DOS effective mass is enhanced through a factor of N_v that does not reduce μ; based on this principle, the S is enhanced without overshadowing the σ.[41,51] Herein, we show that this theory is eclipsed in a low deformation potential (DP) crystal in which the carriers are less scattered by acoustic phonons and thus obtain high mobility. As we find in monolayer WS$_2$ and WS$_2$/WSe$_2$ LS, in spite of the highly degenerate conduction band, the low p-type DP leads to higher hole mobility and therefore the high p-type PF. (ii) Conventional bulk TE materials, such as Bi$_2$Te$_3$ and PbTe, point to that the features of high TE performance should be narrow band gap (high PF) and heavy elements (low κ_l);[48−50] our calculations show that 2D crystals with large band gap and containing a light element also possess comparable zT, which demonstrates that low-dimension can modify the contradiction of TE coefficients. (iii) Finally, it is necessary to note the limitation of our model because the TE transport coefficients especially the κ_l depends strongly on periodic length of the LS. However, relative reports on an in-plane LS structure are rare. According to early reports on bulk Bi$_2$Te$_3$/Sb$_2$Te$_3$,[52] Si/Ge superlattice,[53] and even the Si/Ge superlattice nanowires,[54] the variation of κ_l shows first reduction and latter growth with the increase of periodic length. This bipolar behavior can be understood from two mechanisms, that is, the lattice mismatch introducing anharmonic effect at the interface and depressing the phonon velocities and κ_l; the increase of periodic length, however, gradually lead to a phonon localization with the reduced scattering. Based on Broido and Reinecke,[53] this process can be defined as a competition between the flattened phonon dispersion that inhibits heat conduction and the reduced umklapp scattering that instead enhances it, as the periodic length rises from the ultrathin limit to a larger scale. Therefore, by optimizing the periodic length, one can expect to obtain the best TE performance of superlattice-based bulks or monolayers. In addition, Janus monolayers and their LS were also proposed,[55−59] much lower

κ_l (below 15 W/mK for SMoSe at 300 K)[57] was found as compared to monolayer TMDCs; hence, it is desirable to achieve high TE performance by alloying Janus monolayes with LS.

4. CONCLUSIONS

In summary, we propose to improve the TE performance of 2H TMDC monolayers using LS crystal as the configuration strategy based on the experimental report. The TE transport properties of monolayer WS_2 and WS_2/WSe_2 LS are investigated by DFT combined with the BTE. The underlying origins of electronic transport lie in the electronic band structure consisting of (i) the three-fold degenerate sub-bands that contribute to the high conduction DOS and therefore the high n-type Seebeck coefficient, (ii) the remarkable stair-like DOS relative to the Fermi level accounts for the higher n-type Seebeck coefficient of monolayer WS_2, and (iii) the high p-type σ arising from the extremely high hole mobility leads to the high p-type power factor. In addition, the symmetric electronic transport along zigzag (xx) and armchair (yy) directions can be attributed to the nearly isotropic lifetime of charge carriers. Minimized lattice thermal conductivity in WS_2/WSe_2 LS can be understood from the enhanced anharmonic processes and the weaker bonding stiffness. The phonon anisotropy is explained from the phonon dispersion and group velocity. Due to the remained electronic transport and the minimized lattice thermal conductivity, we achieve the enhanced zT in WS_2/WSe_2 LS with the optimal p-type value exceeding 1 around 400 K. Our results pave the way toward opportunities for enhancing the TE performance of extensive 2D materials by using LS as a building block.

ASSOCIATED CONTENT

ⓈI Supporting Information

The Supporting Information is available free of charge at https://pubs.acs.org/doi/10.1021/acsomega.1c00457.

The results of projected density of states, deformation potential, and electrical thermal conductivity (PDF)

AUTHOR INFORMATION

Corresponding Authors

Guangqian Ding − School of Science, Chongqing University of Posts and Telecommunications, Chongqing 400065, China; ⓞ orcid.org/0000-0002-5676-7097; Email: dinggq@cqupt.edu.cn

Chaochao Dun − Department of Aerospace and Mechanical Engineering, University of Notre Dame, Notre Dame, Indiana 46556, United States; Email: cdun@nd.edu

Xiaotian Wang − School of Physical Science and Technology, Southwest University, Chongqing 400715, China; ⓞ orcid.org/0000-0002-2679-780X; Email: wangxt45@126.com

Authors

Yonglan Hu − School of Science, Chongqing University of Posts and Telecommunications, Chongqing 400065, China

Tie Yang − School of Physical Science and Technology, Southwest University, Chongqing 400715, China; ⓞ orcid.org/0000-0001-8124-7942

Dengfeng Li − School of Science, Chongqing University of Posts and Telecommunications, Chongqing 400065, China; ⓞ orcid.org/0000-0002-4189-400X

Dandan Wu − Institutes of Physical Science and Information Technology, Anhui University, Hefei, Anhui 230601, China

Complete contact information is available at:
https://pubs.acs.org/10.1021/acsomega.1c00457

Author Contributions
#Y.H. and T.Y. contributed equally to this work.

Notes
The authors declare no competing financial interest.

ACKNOWLEDGMENTS

REFERENCES

(1) Li, J.; Li, W.; Bu, Z.; Wang, X.; Gao, B.; Xiong, F.; Chen, Y.; Pei, Y. Thermoelectric Transport Properties of CdxBiyGe1−x−yTe Alloys. ACS Appl. Mater. Interfaces 2018, 10, 39904−39911.

(2) Liu, H.; Zhang, X.; Li, J.; Bu, Z.; Meng, X.; Ang, R.; Li, W. Band and Phonon Engineering for Thermoelectric Enhancements of Rhombohedral GeTe. ACS Appl. Mater. Interfaces 2019, 11, 30756−30762.

(3) Banik, A.; Biswas, K. Lead-free thermoelectrics: promising thermoelectric performance in p-type SnTe1-xSex system. J. Mater. Chem. A 2014, 2, 9620−9625.

(4) He, J.; Kanatzidis, M. G.; Dravid, V. P. High performance bulk thermoelectrics via a panoscopic approach. Mater. Today 2013, 16, 166−176.

(5) Müchler, L.; Casper, F.; Yan, B.; Chadov, S.; Felser, C. Topological insulators and thermoelectric materials. Phys. Status Solidi RRL 2013, 7, 91−100.

(6) Gandi, A. N.; Schwingenschlögl, U. WS2 as Excellent High-Temperature Thermoelectric Material. Chem. Mater. 2014, 26, 6628−6637.

(7) Hicks, L. D.; Dresselhaus, M. S. Effect of quantum-well structures on the thermoelectric figure of merit. Phys. Rev. B 1993, 47, 12727−12731.

(8) Heremans, J. P. Low-dimensional thermoelectricity. Acta. Phys. Pol. A 2005, 108, 609.

(9) Hicks, L. D.; Harman, T. C.; Sun, X.; Dresselhaus, M. S. Experimental study of the effect of quantum-well structures on the thermoelectric figure of merit. Phys. Rev. B 1996, 53, R10493.

(10) Zhang, G.; Zhang, Y.-W. Thermoelectric properties of two-dimensional transition metal dichalcogenides. J. Mater. Chem. C 2017, 5, 7684−7698.

(11) Fei, R.; Faghaninia, A.; Soklaski, R.; Yan, J. A.; Lo, C.; Yang, L. Enhanced thermoelectric efficiency via orthogonal electrical and thermal conductances in phosphorene. Nano Lett. 2014, 14, 6393−6399.

(12) Zberecki, K.; Wierzbicki, M.; Barnaś, J.; Swirkowicz, R. Thermoelectric effects in silicene nanoribbons. Phys. Rev. B 2013, 88, 115404.

(13) Wang, C.; Ding, G.; Wu, X.; Wei, S.; Gao, G. Electron and phonon transport properties of layered Bi2O2Se and Bi2O2Te from first-principles calculations. New J. Phys. 2018, 20, 123014.

(14) Lv, H. Y.; Lu, W. J.; Shao, D. F.; Lu, H. Y.; Sun, Y. P. Strain-induced enhancement in the thermoelectric performance of a ZrS2 monolayer. J. Mater. Chem. C 2016, 4, 4538−4545.

(15) Jin, Z.; Liao, Q.; Fang, H.; Liu, Z.; Liu, W.; Ding, Z.; Luo, T.; Yang, N. A Revisit to High Thermoelectric Performance of Single-layer MoS2. Sci. Rep. 2015, 5, 18342.

(16) Gu, X.; Yang, R. Phonon transport in single-layer transition metal dichalcogenides: A first-principles study. Appl. Phys. Lett. 2014, 105, 131903.

(17) Kumar, S.; Schwingenschlögl, U. Thermoelectric Response of Bulk and Monolayer MoSe$_2$ and WSe$_2$. *Chem. Mater.* **2015**, *27*, 1278−1284.

(18) Duan, X.; Wang, C.; Shaw, J. C.; Cheng, R.; Chen, Y.; Li, H.; Wu, X.; Tang, Y.; Zhang, Q.; Pan, A.; Jiang, J.; Yu, R.; Huang, Y.; Duan, X. Lateral epitaxial growth of two-dimensional layered semiconductor heterojunctions. *Nat. Nanotechnol.* **2014**, *9*, 1024−1030.

(19) Zhang, Z.; Chen, P.; Duan, X.; Zang, K.; Luo, J.; Duan, X. Robust epitaxial growth of two-dimensional heterostructures, multi-heterostructures, and superlattices. *Science* **2017**, 788.

(20) Zhou, J.; Tang, B.; Lin, J.; Lv, D.; Shi, J.; Sun, L.; Zeng, Q.; Niu, L.; Liu, F.; Wang, X.; Liu, X.; Suenaga, K.; Jin, C.; Liu, Z. Morphology Engineering in Monolayer MoS$_2$-WS$_2$ Lateral Heterostructures. *Adv. Funct. Mater.* **2018**, *28*, 1801568.

(21) Zhang, C.; Li, M.-Y.; Tersoff, J.; Han, Y.; Su, Y.; Li, L.-J.; Muller, D. A.; Shih, C.-K. Strain distributions and their influence on electronic structures of WSe$_2$-MoS$_2$ laterally strained heterojunctions. *Nat. Nanotechnol.* **2018**, *13*, 152−158.

(22) Li, F.; Wei, W.; Zhao, P.; Huang, B.; Dai, Y. Electronic and Optical Properties of Pristine and Vertical and Lateral Heterostructures of Janus MoSSe and WSSe. *J. Phys. Chem. Lett.* **2017**, *8*, 5959−5965.

(23) Ding, G.; He, J.; Gao, G. Y.; Yao, K. Two-dimensional MoS$_2$-MoSe2 lateral superlattice with minimized lattice thermal conductivity. *J. Appl. Phys.* **2018**, *124*, 165101.

(24) Zhou, Z.; Fan, D.; Liu, H. Realizing high thermoelectric performance with comparable p- and n-type figure-of-merits in a graphene/h-BN superlattice monolayer. *Phys. Chem. Chem. Phys.* **2019**, *21*, 26630−26636.

(25) Blöchl, P. E. Projector augmented-wave method. *Phys. Rev. B* **1994**, *50*, 17953.

(26) Perdew, J. P.; Burke, K.; Ernzerhof, M. Generalized Gradient Approximation Made Simple. *Phys. Rev. Lett.* **1996**, *77*, 3865−3868.

(27) Kresse, G.; Furthmüller, J. Efficient iterative schemes for *ab initio* total-energy calculations using a plane-wave basis set. *Phys. Rev. B* **1996**, *54*, 11169.

(28) Kim, Y.-S.; Marsman, M.; Kresse, G.; Tran, F.; Blaha, P. Towards efficient band structure and effective mass calculations for III-V direct band-gap semiconductors. *Phys. Rev. B* **2010**, *82*, 205212.

(29) Madsen, G. K. H.; Singh, D. J. BoltzTraP: A code for calculating band-structure dependent quantities. *Comput. Phys. Commun.* **2006**, *175*, 67−71.

(30) Lee, M.-S.; Mahanti, S. D. Validity of the rigid band approximation in the study of the thermopower of narrow band gap semiconductors. *Phys. Rev. B* **2012**, *85*, 165149.

(31) Mahan, G. D.; Sofo, J. O. The best thermoelectric. *Proc. Natl. Acad. Sci. U. S. A.* **1996**, *93*, 7436.

(32) Li, W.; Carrete, J.; Katcho, N. A.; Mingo, N. ShengBTE: A solver of the Boltzmann transport equation for phonons. *Comput. Phys. Commun.* **2014**, *185*, 1747−1758.

(33) Li, W.; Mingo, N.; Lindsay, L.; Broido, D. A.; Stewart, D. A.; Katcho, N. A. Thermal conductivity of diamond nanowires from first principles. *Phys. Rev. B* **2012**, *85*, 195436.

(34) Li, W.; Lindsay, L.; Broido, D. A.; Stewart, D. A.; Mingo, N. Thermal conductivity of bulk and nanowire Mg$_2$Si$_{1-x}$Sn$_x$ alloys from first principles. *Phys. Rev. B* **2012**, *86*, 174307.

(35) Togo, A.; Oba, F.; Tanaka, I. First-principles calculations of the ferroelastic transition between rutile-type and CaCl$_2$-type SiO$_2$ at high pressures. *Phys. Rev. B* **2008**, *78*, 134106.

(36) Feng, T.; Lindsay, L.; Ruan, X. Four-phonon scattering significantly reduces intrinsic thermal conductivity of solids. *Phys. Rev. B* **2017**, *96*, 161201.

(37) Lan, C.; Li, C.; Yin, Y.; Liu, Y. Large-area synthesis of monolayer WS$_2$ and its ambient-sensitive photo-detecting performance. *Nanoscale* **2015**, *7*, 5974−5980.

(38) Huang, J.-K.; Pu, J.; Hsu, C. -L.; Chiu, M.-H.; Juang, Z.-Y.; Chang, Y.-H.; Chang, W.-H.; Iwasa, Y.; Takenobu, T.; Li, L.-J. Large-Area Synthesis of Highly Crystalline WSe$_2$ Monolayers and Device Applications. *ACS Nano* **2014**, *8*, 923.

(39) Ouyang, B.; Chen, S.; Jing, Y.; Wei, T.; Xiong, S.; Donadio, D. Enhanced thermoelectric performance of two dimensional MS$_2$ (M = Mo, W) through phase engineering. *J. Materiomics* **2018**, *4*, 329−337.

(40) Li, W.-F.; Fang, C.; van Huis, M. A. Strong spin-orbital splitting and magnetism of point defect states in monolayer WS$_2$. *Phys. Rev. B* **2016**, *94*, 195425.

(41) Pei, Y.; Wang, H.; Snyder, G. J. Band engineering of thermoelectric materials. *Adv. Mater.* **2012**, *24*, 6125−6135.

(42) Peng, H.; Kioussis, N.; Snyder, G. J. Elemental tellurium as a chiral p-type thermoelectric material. *Phys. Rev.* **2014**, *89*, 195206.

(43) Herring, C.; Vogt, E. Transport and Deformation-Potential Theory for Many-Valley Semiconductors with Anisotropic Scattering. *Phys. Rev.* **1956**, *101*, 944−961.

(44) Hung, N. T.; Nugraha, A. R. T.; Saito, R. Designing high-performance thermoelectrics in two-dimensional tetradymites. *Nano Energy* **2019**, *58*, 743−749.

(45) Hung, N. T.; Nugraha, A. R. T.; Saito, R. Universal curve of optimum thermoelectric figures of merit for bulk and low-dimensional semiconductors. *Phys. Rev. Appl.* **2018**, *9*, No. 024019.

(46) Ma, J.; Li, W.; Luo, X. Intrinsic thermal conductivity and its anisotropy of wurtzite InN. *Appl. Phys. Lett.* **2014**, *105*, No. 082103.

(47) Snyder, G. J.; Toberer, E. S. complex thermoelectric materials. *Nat. Mater.* **2008**, *7*, 105−114.

(48) Tan, G.; Zhao, L. D.; Kanatzidis, M. G. Rationally Designing High-Performance Bulk Thermoelectric Materials. *Chem. Rev.* **2016**, *116*, 12123−12149.

(49) Ding, G.; Li, S.; He, J. Origins of promising thermoelectric performance in quaternary selenide BaAg$_2$SnSe$_4$. *Appl. Phys. Express* **2019**, *12*, No. 071006.

(50) Huang, B.-L.; Kaviany, M. Ab initio and molecular dynamics predictions for electron and phonon transport in bismuth telluride. *Phys. Rev. B* **2008**, *77*, 125209.

(51) Diznab, M. R.; Maleki, I.; Vaez Allaei, S. M.; Xia, Y.; Naghavi, S. S. Achieving an Ultrahigh Power Factor in Sb$_2$Te$_2$Se Monolayers via Valence Band Convergence. *ACS Appl. Mater. Interfaces* **2019**, *11*, 46688−46695.

(52) Venkatasubramanian, R. Lattice thermal conductivity reduction and phonon localizationlike behavior in superlattice structures. *Phys. Rev. B* **2000**, *61*, 3091−3097.

(53) Broido, D. A.; Reinecke, T. L. Lattice thermal conductivity of superlattice structures. *Phys. Rev. B* **2004**, *70*, 081310.

(54) Hu, M.; Poulikakos, D. Si/Ge superlattice nanowires with ultralow thermal conductivity. *Nano Lett.* **2012**, *12*, 5487−5494.

(55) Zhang, J.; Jia, S.; Kholmanov, I.; Dong, L.; Er, D.; Chen, W.; Guo, H.; Jin, Z.; Shenoy, V. B.; Shi, L.; Lou, J. Janus Monolayer Transition-metal Dichalcogenides. *ACS Nano* **2017**, *11*, 8192−8198.

(56) Trivedi, D. B.; Turgut, G.; Qin, Y.; Sayyad, M. Y.; Hajra, D.; Howell, M.; Liu, L.; Yang, S.; Patoary, N. H.; Li, H.; Petrić, M. M.; Meyer, M.; Kremser, M.; Barbone, M.; Soavi, G.; Stier, A. V.; Müller, K.; Yang, S.; Esqueda, I. S.; Zhuang, H.; Finley, J. J.; Tongay, S. Room-Temperature Synthesis of 2D Janus Crystals and their Heterostructures. *Adv. Mater.* **2020**, *32*, 2006320.

(57) Guo, S. D. Phonon transport in Janus monolayer MoSSe: A first-principle study. *Phys. Chem. Chem. Phys.* **2018**, *20*, 7236−7242.

(58) Moreau, P.; Anizon, F.; Sancelme, M.; Prudhomme, M.; Bailly, C.; Sévère, D.; Riou, J.-F.; Fabbro, D.; Meyer, T.; Aubertin, A. M. Syntheses and biological activities of rebeccamycin analogues. Introduction of a halogenoacetyl substituent. *J. Am. Chem. Soc.* **1999**, *42*, 584−592.

(59) Fierke, C. A.; Hammes, G. G. Transient kinetic approaches to enzyme mechanisms. In *Contemporary Enzyme Kinetics and Mechanism*; 2nd ed.; Purich, D., Ed.; Academic Press: New York, 1996; pp. 1−35.